JOURNAL OF COMPUTATIONAL PHYSICS **127,** 218–225 (1996)
ARTICLE NO. 0170

NOTE

An Efficient Fractional-Step Technique for Unsteady Incompressible Flows Using a Semi-staggered Grid Strategy

1. INTRODUCTION

Basically, three distinct approaches are available for solving unsteady incompressible flows; the fractional-step procedure (also called the projection method) [1], a pressure-based method [2], and the method of pseudo-compressibility [3]. Presented here is an expansion of the fractional-step technique of Rai and Moin [4] for fully staggered grids to semi-staggered grids. Rai and Moin demonstrated the highly desirable characteristic of strong numerical stability in their technique using an explicit third-order-accurate Runge–Kutta procedure coupled with explicit high-order-accurate upwind-biased differences for convection. Although their spatial definition was explicit and high-order, high CFL values were still permitted in their computations due to the strong temporal stability of the Runge–Kutta scheme. They emphasized the effectiveness of intrinsic smoothing (via the truncation error) of upwind-biased differencing for contributing towards achieving a robust fractional-step technique.

The primary motivation for expanding their technique to a semi-staggered grid is theoretically based in terms of ensuring that the spatial accuracy along the grid boundaries conforms with the field accuracy. This primary objective is accomplished in three ways. First, the semi-staggered grid eliminates all velocity extrapolation inherent in the fully staggered strategy when adjacent to the grid boundaries. Second, this grid facilitates derivation of a consistent set of boundary conditions for the velocity gradients. Last, no pressure boundary conditions are required to solve the field pressures. To maintain strong coupling between the pressure and velocity components using the semi-staggered grid, we introduce a fourth-order-accurate compact differencing scheme for computing the pressure gradients. This particular development is a key ingredient for extending the fractional-step technique of Rai and Moin to the semi-staggered grid.

For this note, the temporal and spatial discretization of the governing equations and implementation of the solution algorithms and test cases are presented in Cartesian coordinates. The numerical accuracy of the solution methodology and the consistency of the boundary conditions are verified by simulating the decay of periodic vortices. The technique is further verified through comparisons of the experimental and simulation results of a shear-driven cavity flow, as well as cross-flow over a circular cylinder.

2. FORMULATION

The mathematical system which governs unsteady incompressible flows is the Navier–Stokes (NS) equations with continuity. In index notation, the nondimensional form of these equations are

$$\text{Momentum:}\quad \frac{\partial u_i}{\partial t}+\frac{\partial u_i u_j}{\partial x_j}=-\frac{\partial p}{\partial x_i}+\frac{1}{\mathrm{Re}}\frac{\partial^2 u_i}{\partial x_j \partial x_j} \tag{1a}$$

$$\text{Continuity:}\quad \frac{\partial u_i}{\partial x_i}=0, \tag{1b}$$

where the velocity vector $u_i = \langle u, v, w \rangle^{\mathrm{T}}$ and p is the pressure. The Reynolds number is defined as $\mathrm{Re} = \mathrm{UL}/\nu$; ν is the kinematic viscosity and U and L are the characteristic velocity and length, respectively.

The Runge–Kutta/Crank–Nicolson solution sequence extended here to the semi-staggered grid involves three sub-steps ($m = 1, 2, 3$) to update the velocity components and pressure. This sequence introduces an intermediate velocity ($\hat{u}$) that has the form

$$\frac{\hat{u}_i^m-u_i^{m-1}}{\Delta t}=-\alpha^m\left(u_j\frac{\partial u_i}{\partial x_j}\right)^{m-1}-\beta^m\left(u_j\frac{\partial u_i}{\partial x_j}\right)^{m-2}+\frac{\gamma^m}{\mathrm{Re}}\frac{\partial^2(\hat{u}_i^m+u_i^{m-1})}{\partial x_j\partial x_j}, \tag{2a}$$

$$\frac{u_i^m-\hat{u}_i^m}{\Delta t}=-\frac{\partial(\alpha^m\phi^m+\beta^m\phi^{m-1})}{\partial x_i}, \tag{2b}$$

$$p=\phi+\frac{\Delta t}{2\,\mathrm{Re}}\frac{\partial^2\phi}{\partial x_i\partial x_i}, \tag{2c}$$

where $\alpha^m = \langle \frac{8}{15}, \frac{5}{12}, \frac{3}{4} \rangle$, $\beta^m = \langle 0, -\frac{17}{60}, \frac{5}{12} \rangle$, and $\gamma^m = \langle \frac{4}{15}, \frac{1}{15}, \frac{1}{6} \rangle$.

0021-9991/96 $18.00

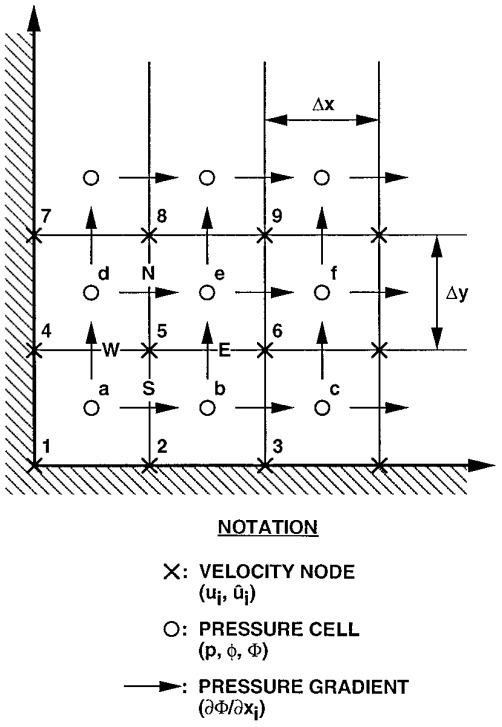

FIG. 1. Computational molecule of the semi-staggered grid.

The velocity components in the intermediate velocity equation at the first sub-step are $u_i^{-1} = 0$ $(m - 2 = -1)$ and $u_i^0 = u_i^n$ $(m - 1 = 0)$. At the third step, $u_i^3 = u_i^{n+1}$ which is the updated velocity for the next time level $n + 1$. A pressure variable ϕ replaces the nondimensional pressure p in the velocity update equation (2b) due to the implicit treatment of the diffusion term. An exact relationship between p and ϕ is given by the simple expression in (2c).

A pressure-Poisson equation can be derived by taking the divergence of the velocity update equation and enforcing continuity (1b). The resultant equation appears as

$$\frac{\partial^2 \Phi^m}{\partial x_i \partial x_i} = \frac{1}{\Delta t} \frac{\partial \hat{u}_i^m}{\partial x_i}, \tag{3}$$

where $\Phi^m = \alpha^m \phi^m + \beta^m \phi^{m-1}$. We note that inasmuch as the intermediate velocity is solved independent of pressure variable, it is not necessary to treat the Runge–Kutta coefficients explicitly. A second scalar variable (Φ) is therefore introduced from which the original nondimensional pressure can be computed anytime during the computation.

3. COMPUTATIONAL MOLECULE

The two-dimensional (2D) computational molecule of the semi-staggered grid shown in Fig. 1 has the velocity components collocated with the grid points (i, j) and the pressure variable computed at the cell centers $(i \pm \frac{1}{2}, j \pm \frac{1}{2})$. In the present technique, the diffusive terms are treated using standard second-order central differences and the convective terms are spatially discretized by a third-order-accurate, five-point, upwind-biased stencil. This stencil has the form

$$\left(\frac{\partial u}{\partial x}\right)_i = \frac{1}{6\,\Delta x}(2u_{i+1} + 3u_i - 6u_{i-1} + u_{i-2}), \quad u_i > 0, \tag{4a}$$

$$\left(\frac{\partial u}{\partial x}\right)_i = \frac{1}{6\,\Delta x}(-2u_{i-1} - 3u_i + 6u_{i+1} - u_{i+2}), \quad u_i < 0, \tag{4b}$$

for the u-component of convection evaluated at grid point i. Its conditional stability characteristics for the linear convection equation are shown in Fig. 2; $\sigma \leq \sqrt{3}$. As pointed-out by Rai and Moin [4], this particular stencil offers implicit smoothing as given by the leading fourth-order truncation error. This artifact is especially useful where high-order artificial dissipation is sometimes necessary to sustain convergence on a coarse grid.

In the pressure-Poisson equation, the Laplacian and divergence operators are discretized by second-order central differences. The intermediate velocities needed at the cell interfaces (see Fig. 1) are determined only through linear interpolation because higher-order functions had a negligible effect on the pressure convergence and its solutions. At the cell faces coincident with the geometric boundaries, the pressure gradient and corresponding intermediate velocity are replaced by the actual boundary velocity value by virtue of the velocity update equation. Thus, pressure boundary conditions in the semi-staggered grid are eliminated. Finally, we applied the modified strongly implicit (MSI) scheme [5] to solve for the intermediate velocities as well as converge the pressure-Poisson equation to a specified error tolerance.

Proper coupling between the pressure and velocity components is critical in the solution methodology and is delivered in the fractional-step technique by the discretization scheme selected for the velocity update equation (2b). If the pressure gradient in this equation is evaluated through second-order interpolation, the cell pressures will decouple from their adjacent neighbors [6]. To avert this dilemma, we compute the pressure gradients at the cell interfaces first (indicated as the arrows in Fig. 1) by a fourth-order-accurate compact differencing formula. The pressure gradients at the grid points are determined by interpolating the appropriate values at the adjacent cell interfaces. For uniform spacing (Δx), the standard formula of this scheme at a point i is [7]

$$\alpha_{i+1} + a\alpha_i + \alpha_{i-1} = \frac{b(\phi_{i+1} - \phi_{i-1})}{\Delta x}, \tag{5}$$

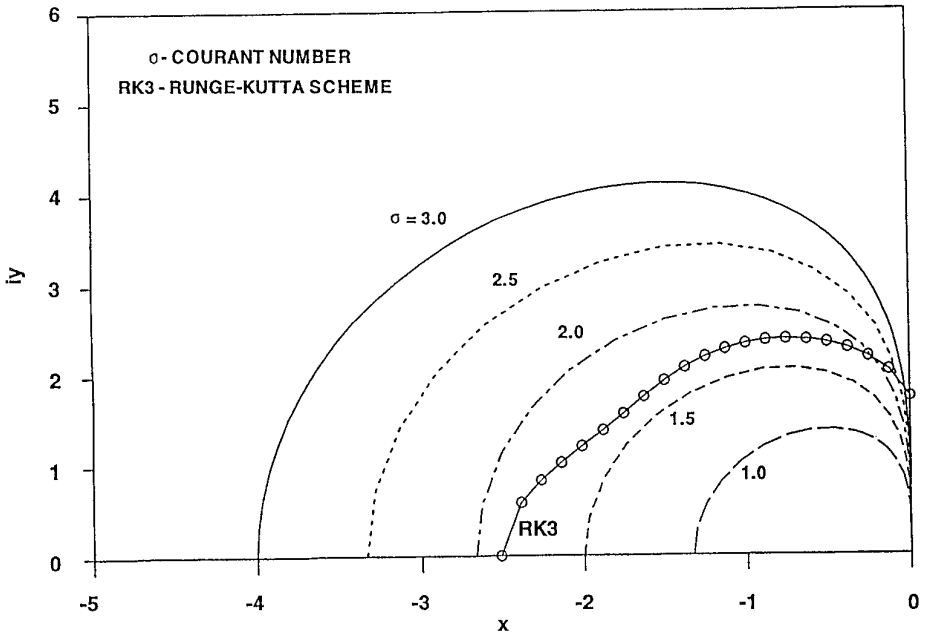

FIG. 2. Numerical stability of the linear convection equation using the third-order-accurate, three-step, Runge–Kutta procedure and third-order-accurate, upwind-biased spatial differences.

where the arbitrary gradient α is $\alpha = \partial\phi/\partial x$ and the coefficients are $a = 4$ and $b = 3$. Application of this scheme to the computational molecule shown in Fig. 1 yields coefficients $a = 22$ and $b = 24$. For example, at the cell interface labeled S

$$f_{i+1}^m + 22f_i^m + f_{i-1}^m = \frac{24(\Phi_{i+1/2}^m - \Phi_{i-1/2}^m)}{\Delta x}, \tag{6}$$

where f_i^m is the pressure gradient in the x-direction; i.e., $f_i^m = (\partial\Phi^m/\partial x)_i$. The index i symbolizes the center point at cell interface S and $i + \frac{1}{2}$ denotes the cell center marked (b). The required boundary conditions are directly available from the respective velocity update equation. In this example, the definition would be

$$\frac{(u_{i-1}^m - \hat{u}_{i-1}^m)}{\Delta t} = -\left(\frac{\partial\Phi}{\partial x}\right)_{i=1}^m = -f_{i-1}^m, \tag{7}$$

where u_{i-1}^m and $\hat{u}_{i-1}^m$ are the interpolated velocity boundary values centered between grid points 1 and 4. Evaluating the pressure gradients for updating the remaining velocity components along with the respective boundary conditions is done in an analogous manner.

One can see that this compact scheme leads to an algebraic set of equations which can be solved by a conventional tridiagonal solver. Because the boundary conditions for this compact scheme are supplied by the velocity update equation, no loss of solution accuracy is introduced at the grid boundaries. The overall spatial accuracy of the compact scheme in terms of evaluating the pressure gradient at the cell interfaces remains fourth order. Finally, by computing the pressure gradients in this manner, we assert that the velocity components and pressure variable remain strongly coupled. Also, no superfluous errors are introduced because the accuracy of the pressure gradients are within the leading truncation error of the overall solution technique.

Establishing boundary conditions for the intermediate velocity in the fractional-step technique can be problematic when employing fully staggered grids. Kim and Moin [8] noted this aspect of time-splitting techniques as a common source of ambiguity when combined with fully staggered grid strategies. For the semi-staggered grid strategy, a proper definition along wall boundaries can be obtained easily by simply projecting Equation (2a) onto the wall. The result is

$$\hat{u}_i^m - u_i^{m-1} = \frac{\gamma^m \Delta t}{\mathrm{Re}} \frac{\partial^2(\hat{u}_i^m + u_i^{m-1})}{\partial x_j \partial x_j}, \tag{8}$$

which is implicit in $\hat{u}_i^m$. By retaining the temporal accuracy of the Crank–Nicolson scheme for the diffusive term, this boundary condition is accurate to $O(\Delta t)^3$.

4. RESULTS

The second-order temporal and spatial accuracy of the solution methodology as well as the consistency of the

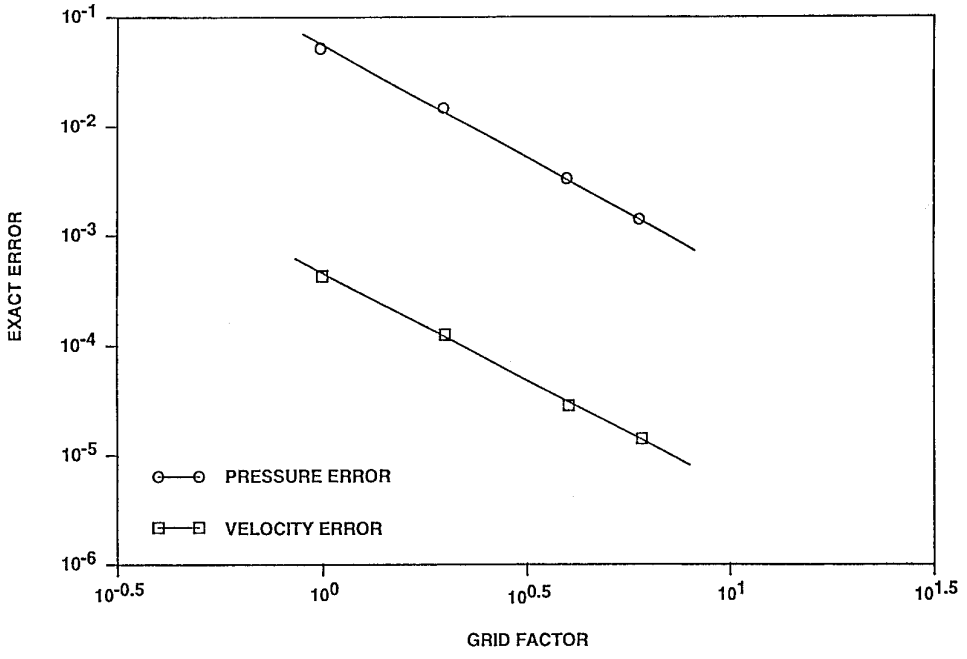

FIG. 3. Improvement in the exact errors of velocity and pressure with grid refinement for a constant courant number.

intermediate velocity boundary conditions can be verified by simulating the decay of periodic vortices. The exact solution describing the decay of periodic vortices has the form [1]

$$u(x, y, t) = -\cos(x)\sin(y)e^{-2t} \tag{9a}$$

$$v(x, y, t) = \sin(x)\cos(y)e^{-2t} \tag{9b}$$

$$p(x, y, t) = -\tfrac{1}{4}[\cos(2x) + \cos(2y)]e^{-4t}. \tag{9c}$$

The simulation was initialized by the exact solution at time $t = 0.0$ and the spatial domain was defined as $0 \leq x, y \leq \pi$. The results of the simulation at time $t = 0.35$ are plotted in Fig. 3, where the grid factor is the ratio of the grid spacing in the reference grid (11×11 uniform) to the refined grid. The exact error was determined as the absolute maximum difference between the exact and numerical solutions normalized by the maximum value in the domain. A linear reduction of the velocity and pressure errors was achieved by refining the grid with a slope of both curves being 2. This test indeed signifies second-order accuracy of the overall truncation error.

We will now present simulation results a 2D steady shear-driven cavity flow (Re = 1000), a corresponding 3D unsteady cavity flow (Re = 3200) and a 2D cross-flow over a circular cylinder (Re = 200). The flow in these three test cases is fully laminar. We performed 2D cavity flow computations to assess the numerical stability and accuracy of the fractional-step technique using very coarse grids as well as its ability to satisfy convergence through grid refinement. In the discussion of the 3D cavity flow results, we include qualitative and quantitative comparisons to the experimental data previously published. The cylinder flow computations will demonstrate the technique's ability to accurately predict a complex unsteady flow.

In each of the cavity flow simulations, the geometry was modeled with unit width (W) and unit height (H). Since the flow visualization data [9] revealed symmetry about the mid-span, the span length (L) in the 3D computations was $L = 1.5W$ giving a spanwise aspect ratio SAR = 3.0; SAR = $2L/W$. The cavity lid moved horizontally at unit velocity and the no-slip condition was applied to all boundaries except the mid-span plane which was treated numerically as a plane of symmetry. An error tolerance of 10^{-5} (L_2 norm) in the pressure residual was found acceptable for satisfying the incompressibility constraint.

For the 2D grids tested, the computations remained convergent using CFL = 2.4. In Fig. 4, we show centerline horizontal velocity profiles from the cavity bottom to the lid. For a 16×16 uniform grid, the present scheme produced a smooth stable solution, whereas second-order central differences gave oscillatory results particularly near the cavity lid where the horizontal velocity gradients are most severe. The present scheme also produced a smooth profile for a 13×13 uniform grid which clearly demonstrates its strong numerical stability even for a very coarse spatial resolution. Grid convergence of the technique is shown in Fig. 5. The computation for a 55×55 uniform

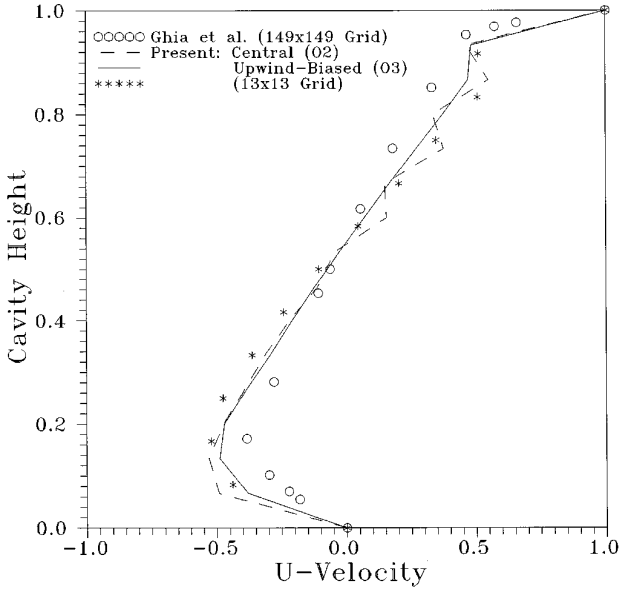

FIG. 4. Results of the 2D steady shear-driven cavity flow computations. Centerline *U*-velocity profiles taken from Ghia *et al.* [10] and the present scheme using either upwind-biased or central differences for convection.

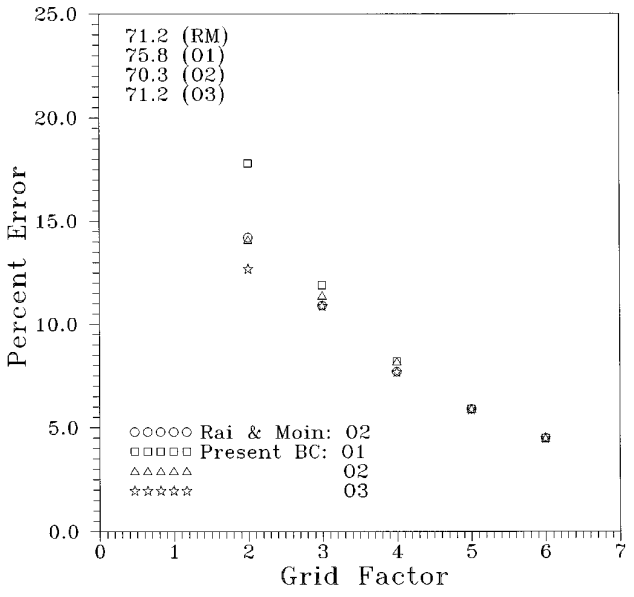

FIG. 6. Prediction of upstream separation point using central and upwind-biased (with extrapolation) differences for convection at first point off cavity wall boundaries.

grid gave overall results to within 2% of that reported by Ghia *et al.* [10] who used a 149 × 149 uniform grid and second-order accuracy. The CPU time for these test cases was approximately 6 μs/grid point/time step on a Cray Y/MP platform.

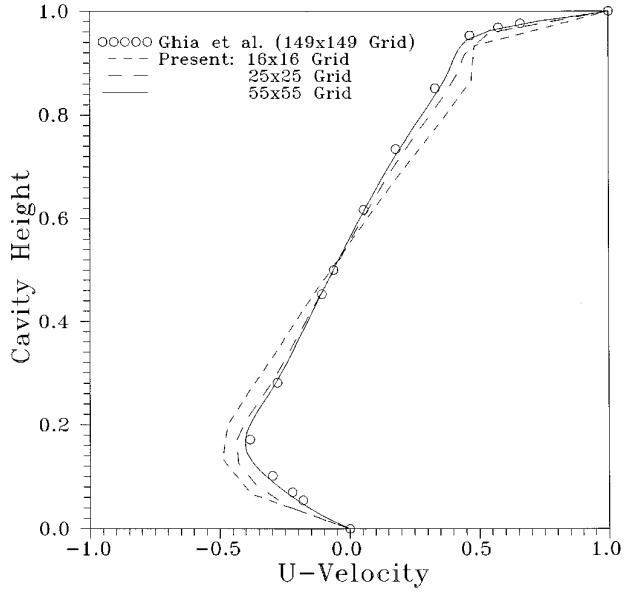

FIG. 5. Centerline horizontal velocity profiles indicating grid convergence of present fractional-step technique for the 2D steady shear-driven cavity flow.

The results plotted in Fig. 6 show four separate approaches for treating the convective terms at the computational points next to the cavity walls; namely, standard second-order central differences (as in Rai and Moin [4]) and upwind-biased differences having first-, second-, and third-order accuracy based on higher-order field extrapolation to obtain the fourth point. For various grid sizes of increasing resolution, we monitored the location of the upstream eddy separation point along the cavity floor. The accuracy of each prediction was gauged by the fine grid solution (149 × 149) of Ghia *et al.* [10]. The grid factor (GF) depicts the ratio of refinement beginning with a 17 × 17 grid. For the intermediate grid sizes, the upstream separation point prediction clearly improved by increasing the spatial accuracy of the convective terms which emphasizes the importance of maintaining a consistent numerical accuracy throughout the entire computational domain.

A 51 × 51 × 65 uniform grid was used for the test case at Re = 3200 with a CFL value of 1.5. As shown in Fig. 7, we predicted four Taylor–Gortler-like vortex pairs spanning the cavity bottom which is in agreement with the experimental observations [9]. The time-averaged ($T = tU/L = 1080$) u-velocity profile through the cavity center at the mid-span are compared with the published experimental data in Fig. 8. Also included in the figure are the 2D steady velocity profiles for a 51 × 51 uniform grid and the previously reported computational results for a 32 × 32 × 45 non-uniform grid [11]. The comparison between the 3D computation and experimental results are quite good, whereas the comparison between the 2D computa-

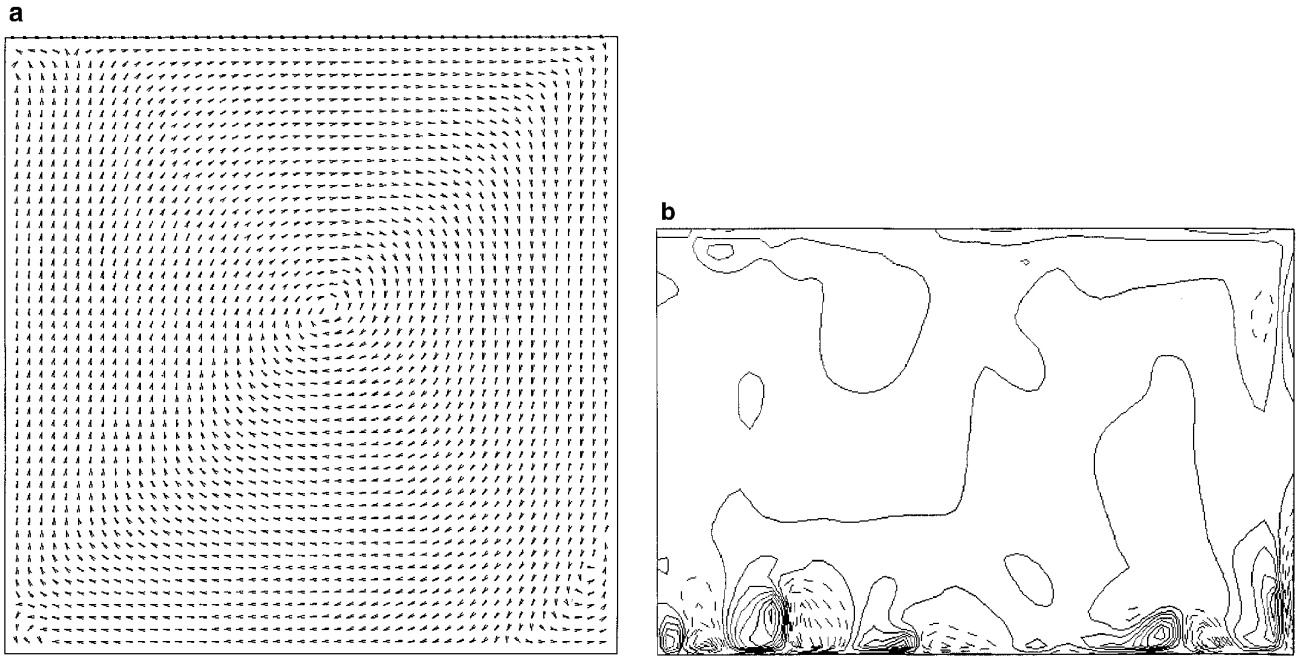

FIG. 7. Snapshot of the recirculation (a) and spanwise flow (b) ($T = 12.0$) of the 3D shear-driven cavity at Re = 3200. Recirculation vectors shown at the cavity mid-span with unit length. Vorticity contours shown of spanwise flow at plane $X = 0.77$. Dashed contours depict clockwise rotation.

tion and the 3D results are quite poor. The significant differences between the 2D and 3D mean velocity profiles are due to the energy drain of the span end-walls on the recirculation flow. Also, our time-averaged velocity profiles away from the cavity side-walls agree better with the experimental data than the corresponding results in [11] because the referenced field resolution was sacrificed by clustering lines closer to the cavity walls in the recirculation planes. As a final note, the CPU requirement was approximately 13 μs/grid point/Runge–Kutta sub-step on a CRAY-Y/MP platform.

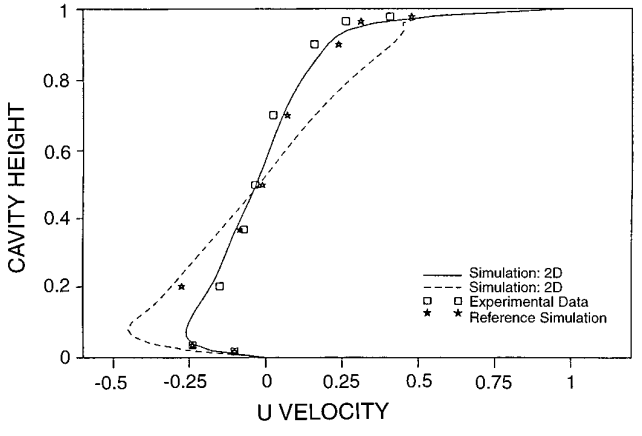

FIG. 8. Comparison of experimental and computational time-averaged U-velocity profiles through the cavity center at the mid-span for Re = 3200. Experimental data taken from Koseff and Street [9] and reference simulation for *Freitas et al.* [11].

For the circular cylinder problem (121 × 99 grid), the exterior limit was fixed at six diameters. The flow was impulsively started with a unit velocity ($U_\infty = 1$) and a zero reference pressure along all grid boundaries except downstream. At exit, zero normal conditions were enforced. The inner boundary which was the cylinder surface was always no-slip. Total lift and drag force coefficients (C_L and C_P) were determined using

$$C_L = C_{L_p} + C_{L_\omega} \quad C_D = C_{D_p} + C_{D_\omega}, \tag{10}$$

where

$$C_{L_p} = \frac{1}{2}\int_0^{2\pi} P_S D \sin\theta \, d\theta, \quad C_{L_\omega} = \frac{1}{\mathrm{Re}}\int_0^{2\pi} \omega_S D \cos\theta \, d\theta,$$

$$C_{D_p} = \frac{1}{2}\int_0^{2\pi} P_S D \cos\theta \, d\theta, \quad C_{D_\omega} = \frac{1}{\mathrm{Re}}\int_0^{2\pi} \omega_S D \sin\theta \, d\theta,$$

The quantities P_S and ω_S are the pressure and vorticity magnitudes along the cylinder surface, respectively.

The components of lift (C_{Lp} and C_{Lw}) and total lift (C_L)

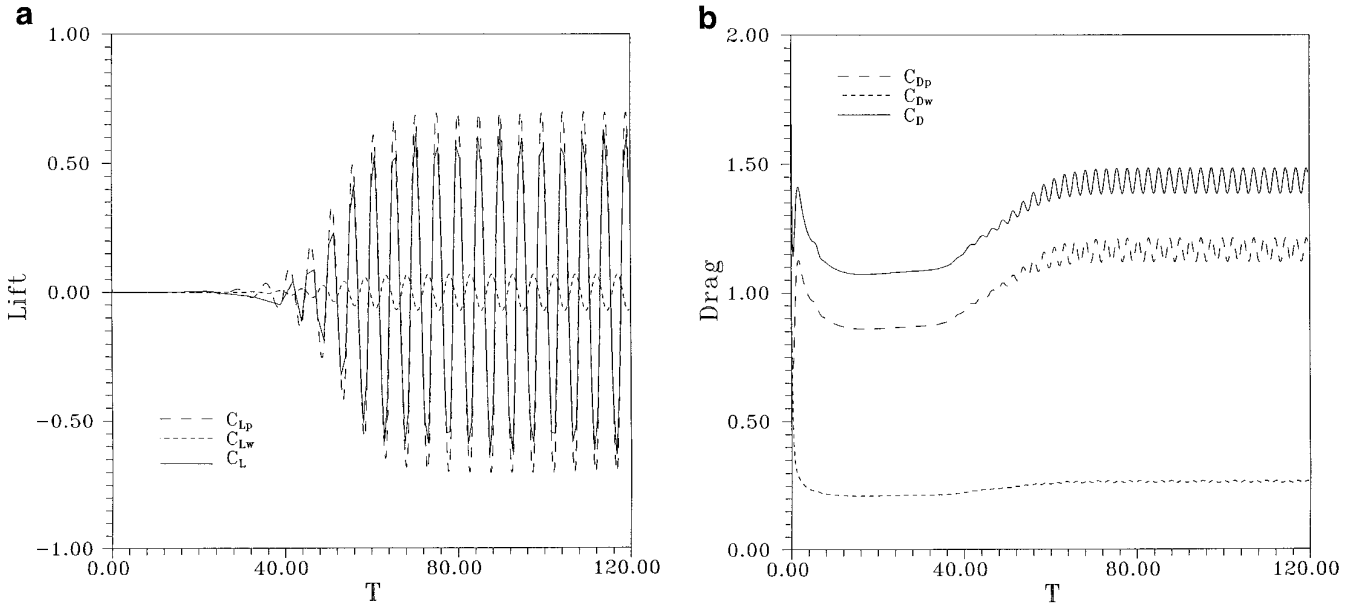

FIG. 9. Profiles of force coefficients during early wake formation of a circular cylinder at Re = 200.

are plotted in Fig. 9a from time $T = 0.02$ (after the initial transients) to time $T = 98.0$; $T = tU_\infty/D$. Total drag and its components over this same period of time are shown in Fig. 9b. Initial signs of an unstable wake appeared at approximately $T = 25.0$ and the transition period from the stable wake to emergence of the vortex shedding phenomena took about 13 time units. Both figures illustrate a moderate growth in the oscillating magnitudes of lift and drag up to their maximums. Beginning at time $T = 38$ (after the transition period), this phase of the wake flow transpire over approximately 32 units of time to $T = 70$. Beyond this time, the near wake is distinctly characterized by a steady oscillatory flow with a Strouhal number of 0.205. Time-averaged values of lift and drag calculated over 7 cycles starting at $T = 70$ are listed in Table I. Experimental determinations, as well as other numerically acquired values, are also listed. Agreement between the present computed force coefficients and the others is acceptable.

TABLE I

Comparisons of Lift (C_L) and Drag (C_D) Coefficients and Strouhal Number (S_t) for Cross Flow over a Circular Cylinder at Re = 200

Reference	C_D	C_L	S_t
12			0.18–0.20
13	1.3		
14	1.46	0.70	0.23
15	1.31	0.65	0.20
Present	1.43	0.68	0.205

5. CONCLUSIONS

The fractional-step technique of Rai and Moin [4] for predicting three-dimensional unsteady incompressible flows using a fully staggered grid strategy was successfully extended to semi-staggered grids. In the semi-staggered grid pattern, pressures are computed at the cell centers and the velocities are collocated with the grid points. Discretizing the governing equations is straightforward and no extrapolation or reflection of the field data is necessary to obtain fictitious velocities lying outside the grid boundaries (as in fully staggered grids). Consistent boundary conditions for the intermediate velocity components were derived and no boundary conditions were necessary for solution of the pressure equation. The difficulty of insuring proper local coupling between the pressure and velocity components was satisfied by computing the pressure gradient in the velocity update equation at the cell faces using a fourth-order-accurate compact differencing scheme.

We verified the solution accuracy of the technique (second order in time and space) through comparisons to an exact solution involving prediction of the decay of periodic vortices. Satisfactory grid convergence was demonstrated in the traditional way through spatial refinement in the solution of a 2D steady shear-driven cavity flow. We showed improvement in the prediction of the cavity upstream separation point by ensuring a consistent spatial accuracy throughout the whole computational domain.

The technique correctly predicted four Taylor–Gortler-like vortex structures spanning the cavity floor of a 3D unsteady cavity flow. Time-averaged results of the cavity centerline horizontal and vertical velocities at the mid-span showed good agreement with the published experimental data. Last, the technique accurately predicted the Strouhal number and force coefficients of a crossflow over a circular cylinder.

ACKNOWLEDGMENTS

The first author gratefully acknowledges the support of the Office of Naval Research (Dr. L. P. Purtell, Scientific Officer) and the Independent Research/Independent Engineering Development Program (Dr. K. Lima, Coordinator) at the Naval Undersea Warfare Center Division Newport. The second author has been supported by the Office of Naval Research, under grant No. N00014-91-J-1233.

REFERENCES

1. A. J. Chorin, *Math. Comput.* **23,** 745 (1969).
2. R. I. Issa, *J. Comput. Phys.* **62,** 40 (1985).
3. W. Y. Soh and J. W. Goodrich, *J. Comput. Phys.* **79,** 113 (1988).
4. M. M. Rai and P. Moin, AIAA-89-0369 (unpublished).
5. S. A. Jordan, *Comput. Fluids* **21**(4), 503 (1992).
6. C. R. Maliska and G. D. Raithby, *Int. J. Numer. Methods Fluids* **4,** 519 (1984).
7. D. A. Anderson, J. C. Tannehill, and R. H. Pletcher, *Computational Fluid Mechanics and Heat Transfer* (Hemisphere, Washington, DC, 1984).
8. J. Kim and P. Moin, *J. Comput. Phys.* **59,** 308 (1985).
9. J. R. Koseff and R. L. Street, *J. Fluids Eng.* **106,** 390 (1984).
10. U. Ghia, K. N. Ghia, and C. T. Shin, *J. Comput. Phys.* **48,** 387 (1982).
11. C. J. Freitas, R. L. Street, A. N. Findikakis, and J. R. Koseff, *Int. J. Numer. Methods Fluids* **5**(6) 561 (1985).
12. J. H. Gerrard, *Philos. Trans. R. Soc. London Ser. A* **288,** 358 (1978).
13. R. Wille, "Karman Vortex Streets," in *Adv. Appl. Mech.*, Vol. 6 (Academic Press, New York, 1960). p. 273.
14. Y. Lecointe and J. Piquet, *Comput. Fluids* **12**(4), 255 (1984).
15. M. Rosenfeld, D. Kwak and M. Vinokur, NASA Tech Briefs ARC-12621, Ames Research Center, Moffett Field, CA, 1993.

Received September 13, 1995; revised January 25, 1996

Stephen A. Jordan
Naval Undersea Walfare Center
Code 8322, Bldg. 1246
Newport, Rhode Island 02882

Saad A. Ragab
Department of Engineering Science and Mechanics
Virginia Polytechnic Institute and State University
Blacksburg, Virginia 24061